Flow control with active dimples

S. Dearing, S. Lambert and J. Morrison
Dept of Aeronautics
Imperial College
London, UK

ABSTRACT

The long-term goal is to design and manufacture optimal 'on-demand' vortex generators, 'dimples' that can produce vortices of prescribed strength and duration for the real-time control of aerodynamic flows that are either undergoing transition or are fully turbulent, attached or separating. Electro-active polymers (EAP) are ideal for a dimple control surface, offering high strain rate, fast response, and high electromechanical efficiency. EAP can also be used as the basis of a resistanc – or capacitance – change pressure sensor, development of which has just begun. In terms of manufacture, inkjet printing of EAP also offers a paradigm shift such that a monolithic control surface is a very real possibility. Important features for integration into a control system are robustness and a predictable, repeatable motion. With these objectives in mind, the suitability of EAP-based actuators is assessed both mechanically and aerodynamically. The ultimate goal is to integrate these devices, along with shear-stress and pressure sensors and distributed control, also under development, into a flexible 'smart skin' which could be incorporated into an airframe structure. The response of a laminar boundary layer to forcing is investiagted using mechanical dimples.

1.0 INTRODUCTION

Generally, aircraft fly in a turbulent flow regime with 50% of cruise drag arising from skin friction[1] and there are very significant environmental and commercial incentives for reducing this. The present paper reports progress in the development of electro-active polymers (EAP)[2] as the basis of an actuator of variable planform that generates time-dependent depressions, 'dimples'. There has been recent progress[3-6] in using EAP circular dimples in experiments beneath laminar boundary layers where the dimple comprises a diaphragm that executes harmonic motion (as would be required of an open-loop control process), or can be made to move transiently when required, a so-called 'on-demand' vortex generator. In this case, we require the dimple to produce a single vortex of known strength for as long or as short a time as required, and the dimple may be generalised to be a time-dependent depression of more-or-less any planform. Their application necessitates an understanding of the basic fluid response and of the electromechanical coupling so that a feedback model for closed-loop control may be implemented. Initial studies on the effects of dimple forcing (variable diaphragm shape, frequency and amplitude) have been completed[3,4] and further results are available from direct numerical simulations[5,6] which are rather more directed towards the development of closed-loop control models. In all these cases, top-dead centre of any transient or harmonic motion brings the dimple flush with the adjacent surface. Other related work involves the use of EAP as a time-dependent textured surface: a layer of harmonically forced EAP is used to generate spanwise travelling waves that are known to reduce turbulent skin-friction drag by as much as 30%. Requirements for control of a turbulent boundary layer suggest[7] that the actuators need to be 10-1,000μm in size, and in the present work, actuation is effected with out-of-plane displacements of approximately 10% of their diameter. The essential ideas and their application to the control of boundary layers are outlined in[8,9]. In particular, ink-jet printing offers a paradigm shift for fabrication which is otherwise expensive

Paper No. 3174. This is an invited paper published to celebrate the 100th anniversary of Imperial College, London.

https://doi.org/10.1017/S0001924000004887 Published online by Cambridge University Press

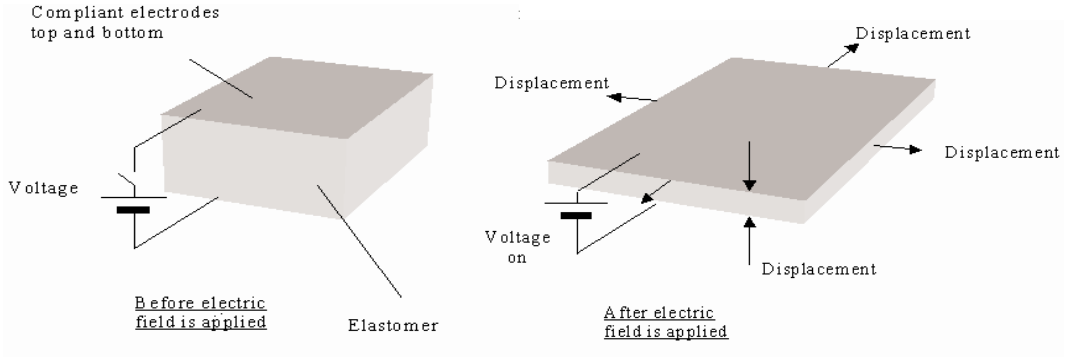


Figure 1. Principle of Actuation.

and time-consuming[9]. Moreover, ink-jet printing is consistent with the use of graphite-based electrodes, and also with the incorporation of carbon nanotubes, which can be made to be both conducting and semi-conducting. A possible alternative, which lends itself well to the use of EAP, is the incorporation of organic semi-conductors in the ink-jet printing process[10]. Given the sensing capabilities of EAP, a monolithic EAP-based 'intelligent' surface for active flow control becomes a very real possibility.

The effects of actuation on the boundary layer may be described by the changes to the vorticity flux due to the actuation. Lighthill[11] has defined an expression for the flux of vorticity, – , from a plane, non-porous stationary surface as:

$$\sigma = \nu(\mathbf{n}.\nabla\omega)_w \qquad \ldots (1)$$

where **n** is the unit wall-normal vector pointing out of the flow domain. He also showed that vorticity flux is balanced by surface pressure gradients:

$$\sigma_z = -\nu\left(\frac{\partial\omega_z}{\partial y}\right)_w = \left(\frac{1}{\rho}\frac{\partial p}{\partial x}\right)_w \qquad \ldots (2)$$

$$\sigma_x = -\nu\left(\frac{\partial\omega_x}{\partial y}\right)_w = -\left(\frac{1}{\rho}\frac{\partial p}{\partial z}\right)_w \qquad \ldots (3)$$

where p is the pressure, ρ is density and ω_x and ω_z are, respectively, the streamwise and spanwise components of vorticity. The y-direction is normal to the surface (pointing inwards). These equations are readily obtainable from the Navier-Stokes equations at the wall. Subsequently, Wu *et al*[12,13] have derived the vorticity-flux equation from a moving surface of arbitrary shape:

$$\sigma = \mathbf{n}\times\mathbf{a} + \mathbf{n}\times\frac{\nabla p}{\rho} - \left(\mathbf{n}\times\tau_w\right)\cdot\mathbf{K} - \mathbf{n}\left(\mathbf{n}\cdot\left(\nabla\times\tau_w\right)\right) \qquad \ldots (4)$$

where τ_w is the wall shear stress. On the right hand side, the first three terms represent the generation of vorticity flux by surface acceleration, **a**, pressure gradient and surface curvature, respectively ('ascending mechanisms')[12]. The curvature tensor is $\mathbf{K} = -\nabla_\pi\mathbf{n}$, with ∇_π being the tangential component of the nabla operator. The last term of the equation, the shear-stress gradient, is the 'upturning mechanism'[12], which is a viscous diffusion term that creates wall-normal vorticity as a consequence of the solenoidal condition, $\nabla_\omega = 0$.

The vorticity flux equation is very useful in helping to identify those aspects of a boundary responsible for the generation of vorticity flux. Furthermore, it indicates that all the sources of flux are mutually dependent, and that, for example, wall acceleration affects the distribution of pressure and skin friction on the wall. In the case of a plane-surface dimple with motion in the surface-normal direction only (so that it generates a vertical-sided depression – one of the cases considered in detail here), the acceleration source term is identically equal to zero but the pressure-gradient source term is non-zero. The curvature term is also zero except at the piston edges where the curvature becomes infinite and where separation is inevitable once the dimple is depressed. For a dimple generated by a depressed diaphragm on which the curvature is continuous, separation becomes dependent primarily on Reynolds number and on the depth of the depression, and the curvature source term is bounded and variable. The response to a second type of 'smooth' dimple forcing is also examined below. Moreover, where the surface acceleration is not parallel to the surface normal, additional flux generation may result from the acceleration source term. It is also important to note that, as in the present case, measurements of vorticity in an Eulerian frame, as done here, should be compared with equation[4] in which the acceleration includes the convective term[6]:

$$\mathbf{a} = \frac{\partial u}{\partial t} + \left(\mathbf{u}\cdot\nabla\right)\mathbf{u} \qquad \ldots (5)$$

Then equations (2) and (3) become, respectively,

$$\sigma_z = \left(\frac{1}{\rho}\frac{\partial p}{\partial x} + u\frac{\partial u}{\partial x} + v\frac{\partial u}{\partial y}\right)_w \qquad \ldots (6)$$

$$\sigma_x = \left(-\frac{1}{\rho}\frac{\partial p}{\partial z} - v\frac{\partial w}{\partial y}\right)_w \qquad \ldots (7)$$

The same result may be obtained from first principles and the inclusion of acceleration for the moving wall as a pseudopressure[14].

2.0 ELECTRO-ACTIVE POLYMERS

An EAP actuator comprises an elastomer sandwiched between compliant electrodes. They are preferred over alternative actuation systems such as piezoelectric, electrostatic and electromagnetic devices because of their simplicity and good electro-mechanical coupling efficiency and low weight[15]. The elastomer should have low stiffness, be nearly incompressible and have a high dielectric constant and capable of large mechanical strains. Typical values of mechanical strains vary from 67-380% over a broad range of frequencies[16] and the electro-mechanical efficiency is typically about 80%. EAP is also tolerant to a wide range of environments and operates satisfactorily in the temperature range of –65º to 240ºC. Acrylics, for example, do not have the same operational temperature range. An electrostatic pressure, due to an electric field applied across compliant electrodes, causes a thickness strain to the polymer film, which in turn leads to a lateral expansion in area, due to the incompressibility of the elastomer. This is shown schematically in Fig. 1.

https://doi.org/10.1017/S0001924000004887 Published online by Cambridge University Press

The effective mechanical pressure, P, in the surface-normal direction is proportional to the square of the electric field, E, in volts m^{-1}.

$$P = \varepsilon_0 \varepsilon_r E^2 = \varepsilon_0 \varepsilon_r \frac{V^2}{z^2} \quad \ldots (8)$$

where z is the elastomer thickness. The pressure is double the electrostatic pressure of a parallel plate capacitor because the EAP has compliant electrodes, which allow not only coupling of the attractive force between the oppositely charged electrodes but also the repulsive forces separating the charge on the same electrode. The pressure is also dependent on the dielectric constant, the product of the relative dielectric constant of the elastomer, ε_r, which is elastomer dependent and the permittivity of free space, ε_0. It can easily be seen that the physical properties of the material can be tailored to suit the application. The reciprocal mechanism, pressure sensing, is also being developed so that actuation and surface pressure measurement may be accomplished in the same surface. EAP also acts in response to an applied force: a contraction works against the applied electrostatic field and raises the voltage of the charge, thus generating electrical energy. Therefore, the same surface may be used to measure surface pressure.

When an EAP film is bonded to the substrate, the lateral motion is constrained at the edge of the dimple, thereby producing out-of-plane buckling when the voltage is applied, as shown in Fig. 2. Simple mechanical biasing in the form of an additional passive polymer layer ensures that the buckling always leads to a depression.

For the present application, design criteria include a deflection-to-diameter ratio (ε_r/D), of 10%, a frequency response in the kHz regime and downward-only movement (to form a recessed dimple rather than a bump). Given that large electric fields are required (typically, 80MV m^{-1}), larger deflections can be obtained by using thin multiple layers where the total out-of-plane is the sum of the deflection in each layer: for example, 750µm multi-layer (15 × 50µm) stack has been used[17] to achieve higher deflections. In the present work, several silicone elastomers have been considered: Nusil MED10-6607P, MED10-6605P, MED-4905, DOW CORNING SYLGARD 186 and SYGLARD 182. These materials are all silicones but have a different Young's modulus and shore A number. The substrate supporting the micro-actuator devices is a silicon wafer. In order to provide electrical isolation, a 2µm oxide layer was thermally grown on both sides. The elastomer films have been produced by spin coating so that thin films with high homogeneity can be fabricated. The film thickness depends on the rotational speed, spinning duration and viscosity of the elastomer. However, more recently, commercially available samples of variable thickness ($50 < z < 250$µm) have been used.

In order for the actuator to have a sufficiently small stiffness, the electrode must be compliant. Additionally, for this particular application the electrodes must (a), be able to withstand fast dynamic motion, and (b), resist humidity and temperature changes. The use of compliant gold electrodes[9,18] can lead to an overall stiffening of the dimple or lead to delamination. Other approaches are possible:

1. Graphite powder or carbon grease;
2. Conducting elastomer (elastomer loaded with a conducting material). Two variants were investigated; carbon-loaded elastomer (carbon fibre fragments 10µm in diameter and up to 300µm long) and a silver-loaded elastomer (silver particles typically 6µm in diameter). However, at the coating thickness required, the particle and fibres are quite widely spaced and a conductive path is not easily formed.

For these reasons, the present work focuses on the use of graphite electrodes. In this case, uniformity of the dispersed graphite and electrode conductivity (and therefore, homogeneity of the electric field) is important so that motion is both repeatable and predictable.

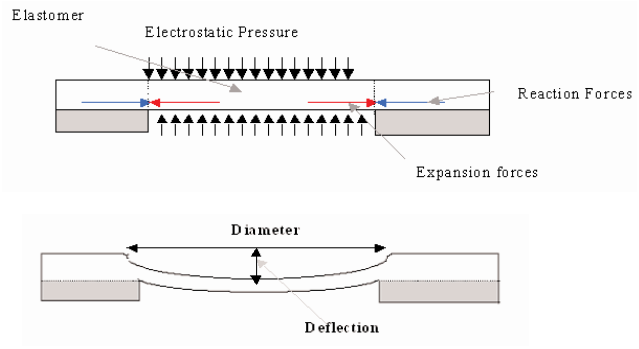


Figure 2. Principle of operation of a dimple.

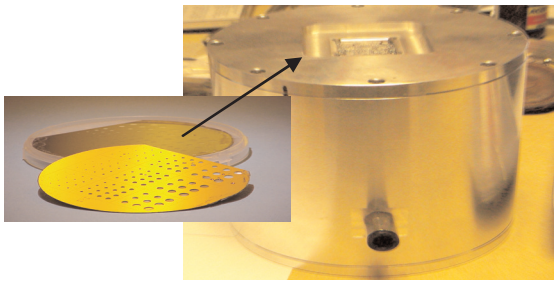


Figure 3. Bulge test equipment.

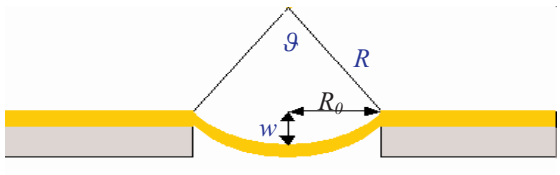


Figure 4. Deflected dimple.

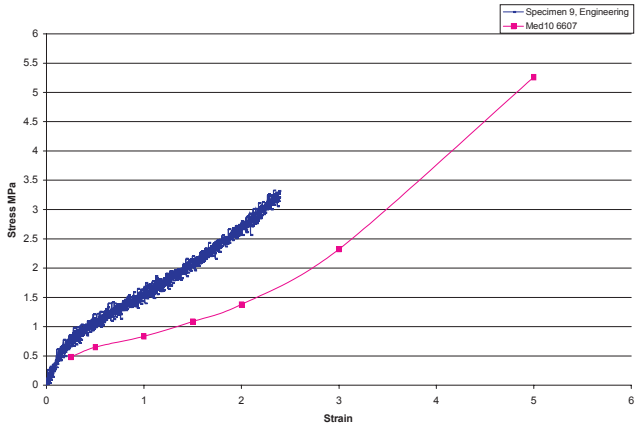


Figure 5. Effect of fabrication process: engineering stress tensile test MED10-6607P: , specimens 1-12, spin-coated to a thickness of 20µm; bulk specimen thickness 685µm.

https://doi.org/10.1017/S0001924000004887 Published online by Cambridge University Press

2.1 Estimation of Young's Modulus

The mechanical strain is directly proportional to the Young's modulus, E, a property sensitive to both fabrication technique and size. For this reason, the strain response of the material is studied using a series of axial and bulge tests. This behaviour can be characterised using constitutive material models. For small strains, Hookean (linear) behaviour can be assumed. The Hooke model predicts the force on the uniaxial sample is proportional to its change in length, and therefore in this case, E is simply determined from uniaxial tests.

Bulge testing is also performed because it provides the same boundary conditions as a dimple. It involves applying biaxial stresses to a material. Pressure is used to deflect an elastomer spun coated onto a silicon wafer which is subsequently etched to produce different size apertures (2mm to 4·5mm), as shown in Fig 3. Displacement is measured using a non-contact optical measurement technique, Digital Speckle Photogrammetry (DSP) which records displacements under load using CCD cameras. For each load, the 3D-coordinates of the object surface are calculated on the basis of digital image processing providing 3D displacements as well as the surface strain.

The general pressure-deflection relationship in the centre of the membrane is given by $P = f(w)$[19]:

$$P = \left(\frac{ER}{2z_0}\right)\left(1+\frac{vw}{R_0^2}\right)^2 \qquad \ldots (9)$$

assuming that the elastomer membrane forms an hemispherical shell for which the strain distribution is based on simple geometrical relationships, Fig. 4. z_0 and R_0 are, respectively, the thickness and radius of the undeflected membrane and w, the out-of-plane deflection. v is Poisson's ratio. Equation (9) may therefore be used to estimate Young's Modulus, E.

Devices with EAP thicknesses in the range 10-40µm have been fabricated by spin coating. It has been found that the material properties for the membrane cannot be extrapolated from bulk relationships. There is an apparent increase in Young's Modulus by an order of magnitude for uniaxial data. Figure 5 shows engineering stress tensile test results for spin-coated MED10-6607P sample, thickness 20µm, for which E = 2·61MPa. The lower curve shows corresponding data from a bulk specimen of thickness 685µm for which E = 2·16MPa. Both stress-strain curves are nonlinear.

Bulge testing has highlighted important design issues. The Young's Modulus for biaxial strain is two orders of magnitude larger than that deduced from uniaxial tests. There is a hysteresis effect; the difference between area under the unloading and loading curves is 22% at maximum load. Also, stress concentrations at the interface of the silicon wafer and the silicone at the aperture edge cause common mode failure.

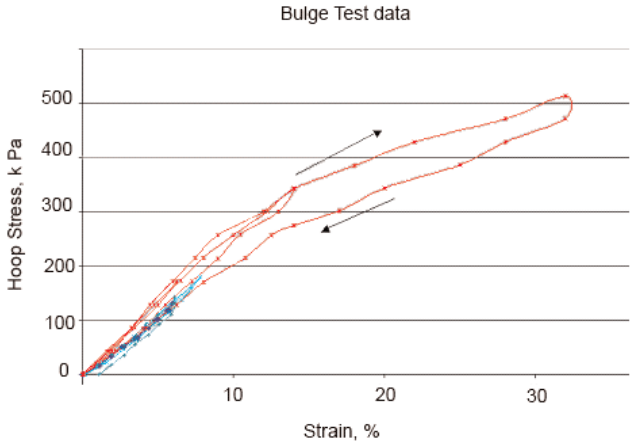


Figure 6. Bulge Test MED10-6607P: hoop stress variation for loading and unloading.

2.2 Calculation of electromechanical coupling efficiency (k)

A key figure of merit of an electromechanical actuator is represented by its k value that quantifies the percentage of electrical energy that is converted into useful mechanical energy. The efficiency is defined as:

$$k = \frac{W_m}{W_e} \qquad \ldots (10)$$

where W_e and W_m are, respectively, electric charging work and generated mechanical work for the same volume of elastomer. W_e can be calculated from the energy generated by charge on a capacitor:

$$W_e = \frac{CV^2}{2} \qquad \ldots (11)$$

V is the steady-state voltage applied to the actuator-equivalent capacitance, C, assumed to be constant with time. Similarly, the work done to achieve a given displacement, $(x - x_0)$, is defined as force multiplied by distance travelled. This is equal to:

$$W_m = \int_{x_0}^{x} F_x \, \mathrm{d}\, x \qquad \ldots (12)$$

2.3 Circular actuator test

Electro-mechanical characterisation is achieved by the testing of a circular membrane. A circular actuator of diameter O (mm), as shown in Fig. 7, was initially employed as a standard test to establish the sensitivity of various types of EAP of varying thickness to a range of electrical field strengths. The polymers pre-strained in the x, y direction and were coated with graphite powder. Pre-straining reduces the thickness of a sample, so increasing its sensitivity.

Table 1 gives a list of pre-strain and estimated thicknesses. The thickness resulting from pre-strain is given by:

$$z = z_0(1 + S_{zz,p}) \qquad \ldots (13)$$

where z_0 is the thickness prior to pre-strain, and $S_{zz,p}$ is the strain in the z direction. Assuming that the elastomer is incompressible, $S_{zz,p}$ can be estimated from:

$$S_{zz,p} = \frac{1}{\sqrt{(1+S_{xx,p})(1+S_{yy,p})}} \qquad \ldots (14)$$

where $S_{xx,p}$ is the measured pre-strain in the x-direction:

$$S_{xx,p} = \frac{x - x_0}{x_0} \qquad \ldots (15)$$

Here x_0 is the pre-stretched length of the specimen. $S_{yy,p}$ is found in a directly analogous way.

Table 1
List of specimen pre-strains and estimated thicknesses for z_0 = 250 µm

Applied (x,y)-pre-strain %	Estimated thickness µm
60	98
122	50
150	40

https://doi.org/10.1017/S0001924000004887 Published online by Cambridge University Press

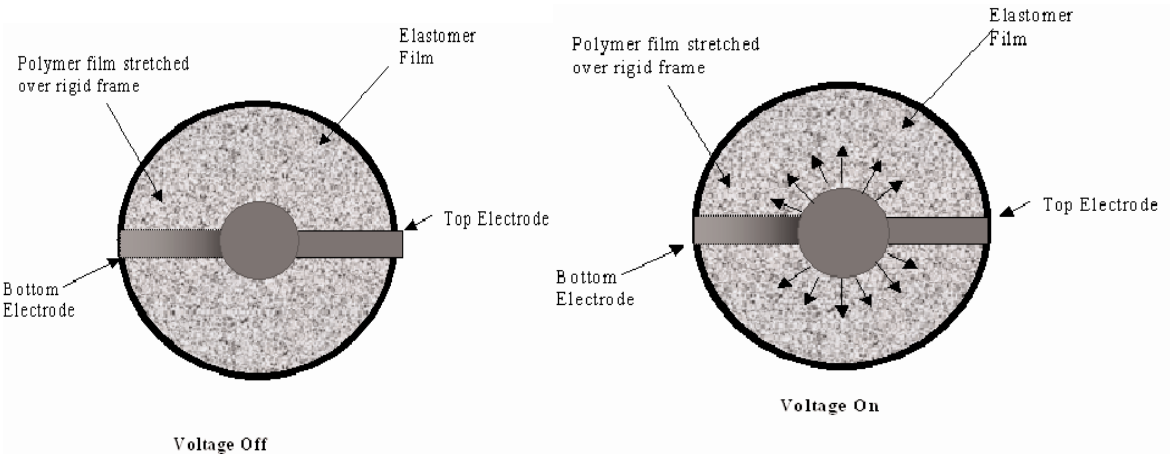


Figure 7. Circular Actuator Test.

Samples are actuated by a.c. and d.c. electric fields and measurements of strain and thickness reduction were measured using the DSP. This equipment is also used to characterise the out-of-plane response for given electric fields of a 'macro sized dimple' as described in Fig 2. For each specimen a two-terminal resistance measurement of the electrode was made as well as the leakage current using a high-voltage probe. These measurements are used to develop an operational 'window' based on dimensionless parameters, in which samples are expected to be free of voltage breakdown and of mechanical failure.

2.4 Measurements of dielectric constant

A high-accuracy capacitance meter was used to make measurements of capacitance for different electrode designs and electrode fabrication techniques. Using the basic relationship for a parallel-plate capacitor of area A and thickness z, as described in Equation (16), an estimate of ε_r for each material can be found:

$$z = z_0(1 + S_{zz,p}) \quad \ldots (16)$$

Samples of MED 10-6607P and MED 4905 were tested for their dielectric constant. It was found to be 2·8 in both cases. Measurements of current permit the estimation of the time constant of the equivalent RC circuit for the elastomer. Use of a large in-line resistance permits estimates of leakage current, sudden increases of which are likely to occur immediately before breakdown.

2.5 Electromechanical properties

Measurements of strain and thickness strain for four different electromechanically loaded materials have been examined for a range of thicknesses. It has been found that electromechanical strain is sensitive to the type of voltage input, material thickness, pre-strain, material properties such as Young's modulus and Shore A value as well as actuator size. For, example, MED-6607P has a Shore A number of 40, which is too large for an electro-mechanical response using up to 4kV excitation. Figure 6 shows results for a.c. voltage and dc modulated excitation for MED4905 (non-spin coated sample) with a pre-strain of 122%. This is equivalent to a thickness of 50μm.

For comparison, an ac electric field, –80MV/m and 80MV/m, Fig 8, gives a maximum thickness reduction of 5·8% compared to 12·8% for –80MV/m dc electric field. This result is 50% less than the expected strain resulting from using an electromechanical pressure based on linear material properties, Equation (8). This could be due to the non-linearities of the material properties, or to non-uniformities in

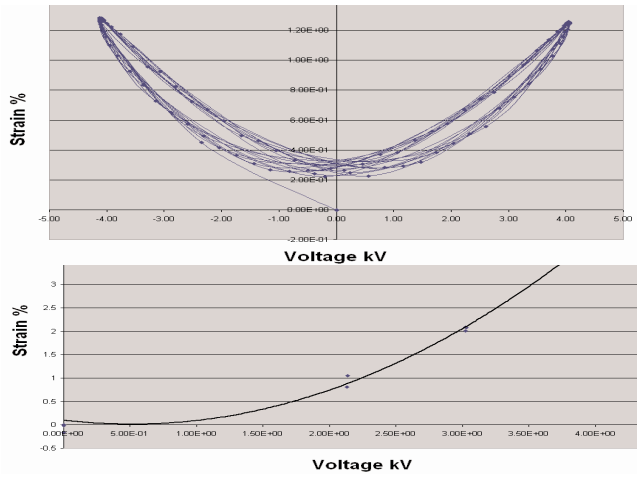


Figure 8. Circular Actuator Results for MED4905. 30mm diameter, 50μm thickness; 122% pre-strain. Top- a.c. voltage +4kV to –4kV applied. Bottom-Modulated dc voltage, +4kV to 0V.

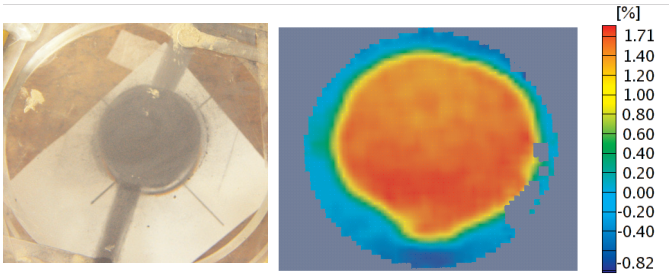


Figure 9. Thickness reduction of a 30mm circular actuator of thickness of 50μm for electric field strength of 30MV/m. Contours show thickness strain.

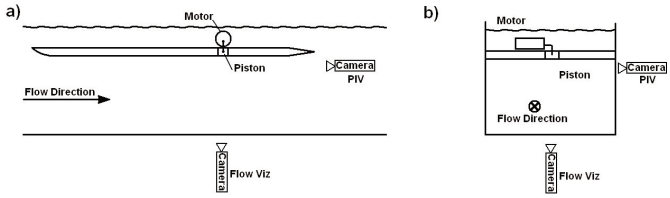


Figure 10. Schematic of experimental arrangement: (a) side view; (b) front view.

https://doi.org/10.1017/S0001924000004887 Published online by Cambridge University Press

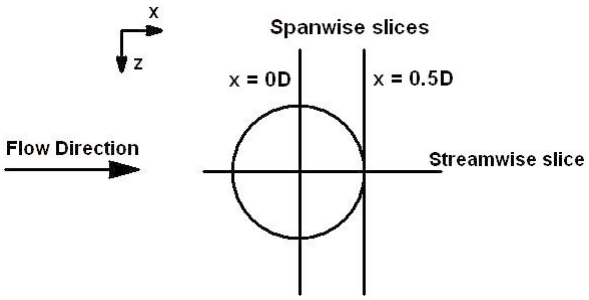


Figure 11. PIV planes. Streamwise (*x,y*) plane and spanwise (*y,z*)planes at *x/D* = 0 and 0·5.

the electric field, causing a non-uniform thickness reduction across the whole circular electrode. The non-uniform electric field can be caused by non-uniform electrode conductivity. Figure 9 shows thickness strain for a 30mm diameter membrane. Taking the deflection to form a hemi-spherical surface, a 4 % radial strain will provide a 339μm out-of-plane deflection for a 3mm dimple, that is, a deflection of about 10%.

3.0 FLUME AND MODEL

Experiments were carried out in a water flume with a cross section of 0·6m by 0·6m and a test-section length of 8·4 m. The flow rate is determined using an electromagnetic Toshiba LF400 flow meter, and the freestream velocity is set at 0·04ms^{-1}, the dimple diameter, D, is 0·016m with maximum amplitude, e, of 0·1D. It is located 1·5m downstream of the leading edge of a 2·2m long flat perspex plate and the forcing frequency is varied between 16Hz and 145Hz. For this condition, $\mathrm{Re}_D = U_\infty D/\nu = 640$ and $\mathrm{Re}_x = U_\infty x/\nu = 60{,}000$. Using the Blasius solution, the laminar boundary-layer thickness is estimated to be $\delta/D = 5x/(D\sqrt{\mathrm{Re}_x}) \approx 2$. The dimensionless forcing frequency (Strouhal number), $\mathrm{St} = f\delta/U$, varies in the range $13{\cdot}0 \le \mathrm{St} \le 112$. The active dimple is driven by an electric motor. The cam shaft which connects the motor to the piston is designed such that there is minimal wear between the piston and the shaft. This is achieved by placing the primary shaft, which is connected to the motor, inside a secondary hollow shaft. The two shafts are separated using ball-race bearings, so that the shear stress is not transmitted between the two shafts. The shaft is long enough to accommodate two pistons separated by up to eight piston diameters.

For the vertical-sided dimple, flow visualisation was performed using dye paste placed on the flat plate upstream of the dimple. The dye paste is made up of potassium permanganate, corn syrup and methanol in a ratio of 1:2:1. The result is a sheet of dye which flows just above the surface and gets deformed by the forcing of the dimple. For the smooth dimple, fluorescein dye was used. The dye sheet deformations were photographed using a three Mpixel digital camera placed beneath the dimple with the view into the dimple.

Table 2
Non-dimensional quantities: Vertical-sided and smooth dimples.

St	S (smooth)	S (vertical-sided)
13·0	21·5	30·4
24·0	29·2	41·3
56·0	40·4	57·2
68·0	49·2	69·5
90·0	56·6	80·0
112·0	63·1	89·2

PIV was performed using a Photron APX camera, a Copper Vapour Laser and ViDPIV software from Oxford Lasers. The camera resolution is 1,024 by 1,024 pixels, and can record up to 2,000 frames per second at maximum resolution. The Copper Vapour laser is synchronised to the camera, the wavelengths of the laser light are 510·6nm (green) and 578·2nm (yellow), with a green-to-yellow intensity ratio of 1·5 to 2. The recording technique used is multi-frame/single exposure. For each run, 2,048 images are acquired, producing 2,047 image pairs. The camera is first placed to the side of the dimple to record streamwise slices of the flow, and then it is placed beneath the flume and directly downstream of the dimple to record spanwise views. The camera can only record at predefined sampling rates and thus cannot be adjusted to the actuation frequency of the piston. However, between 8 and 14 image pairs per cycle are recorded so that each set of results covers between 150 and 250 actuation cycles.

4.0 FLOW VISUALISATION AND PIV RESULTS

Table 2 shows non-dimensional variables used to characterise the two dimple geometries, one vertical-sided, the other smooth. In both cases, the deflection is 10%D, with the result that the volume flux due to the smooth dimple is about half that of the vertical-sided one. Non-dimensional quantities are defined as:

$$\left[\varepsilon^*, St, S, \mathrm{Re}_\tau, \delta^*, \mathrm{Re}_\delta, \mathrm{Re}_D, \mathrm{Re}_x\right] \in \left[\frac{\varepsilon}{D}, \frac{f\delta}{U_\infty}, \sqrt{\frac{u_j D}{\nu}}, \frac{u_\tau \delta}{\nu}, \frac{D}{\delta}, \frac{U_\infty D}{\nu}, \frac{U_\infty x}{\nu}\right] \quad \ldots (17)$$

where S is a Stokes number, $\sqrt{fD^2/\nu}$, which for $\varepsilon = 0{\cdot}1$ and $f\varepsilon \approx u_j$ is equal to $\sqrt{u_j D/\nu}$ is the volume-averaged dimple jet velocity. The remaining parameters in Equation (17) are fixed as the boundary layer is the same for both the vertical-sided and smooth dimple forcing.

4.1 Vertical-sided dimple

For each forcing frequency, three planes of PIV data are shown, one in the streamwise direction along the centerline of the piston and the other in the spanwise direction on the downstream edge of the dimple. Streamwise vorticity contours are non-dimensionalised as $\omega_x^* = \omega_x / f$. Non-dimensional spanwise vorticity contours are evaluated as $\omega_z^* - \omega_{z0}^*$, where ω_{z0}^* is the vorticity of the unforced boundary layer. Velocity vectors are of arbitrary scaling and for illustrative purposes only. At each St, a plan-view visualisation picture is also shown. The origin is located at the centre of the dimple, flush with the testing surface. At low forcing frequencies, some vorticity is apparent that is not generated by the dimple motion. This is because the flume pump is operating quite close to stall at low speeds. The resulting motion has long time-scales which are not apparent at higher forcing frequencies at which the vorticity generated by the dimple dominates. In all vorticity contours, dark (blue) regions of vorticity are negative, and of the same sign as the incoming boundary layer (left to right).

Figures 12, 13 and 14 show flow visualisation time-averaged PIV results at values of St = 24·0, 46·0 and 112·0, respectively. Each one is representative of a distinct regime. St = 24·0, a horseshoe-vortex-like structure is most clearly evident in the Fig. 12(a), and appears to be generated by the viscous blockage caused by the dimple motion. Figure 12(b) shows that negligible spanwise vorticity is generated by the dimple motion while the dimple-generated streamwise vorticity, more clearly evident at $x/D = 0{\cdot}5$, Fig. 12(d), appears weak at $z/D = \pm 0{\cdot}5$. The associated rotation is consistent with the generation of a 'necklace' horseshoe vortex with common flow towards the surface between the legs of the horseshoe vortex.

https://doi.org/10.1017/S0001924000004887 Published online by Cambridge University Press

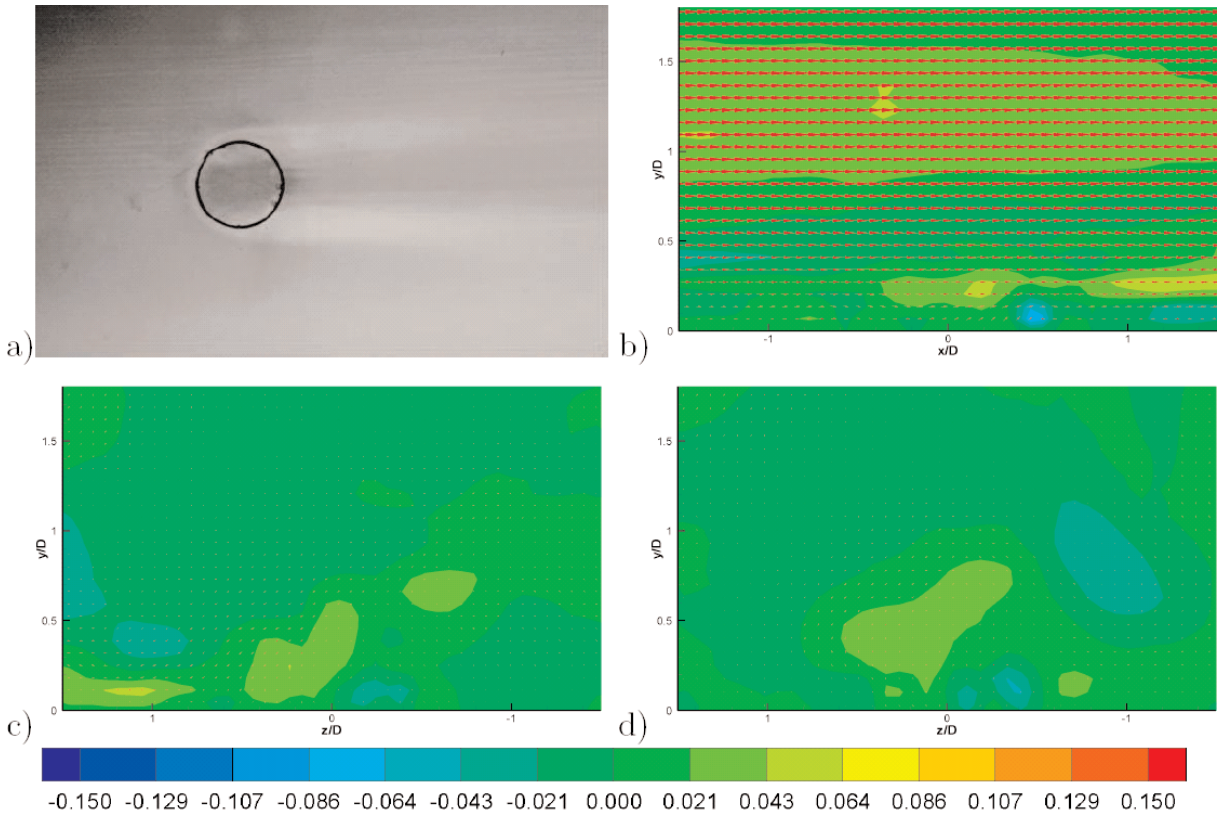


Figure 12. Flow visualisation and time-averaged PIV, St = 24·0.
(a) Flow visualisation; (b) streamwise plane along dimple centre-line; (c) spanwise plane *x/D* = 0; (d) spanwise plane *x/D* = 0·5.

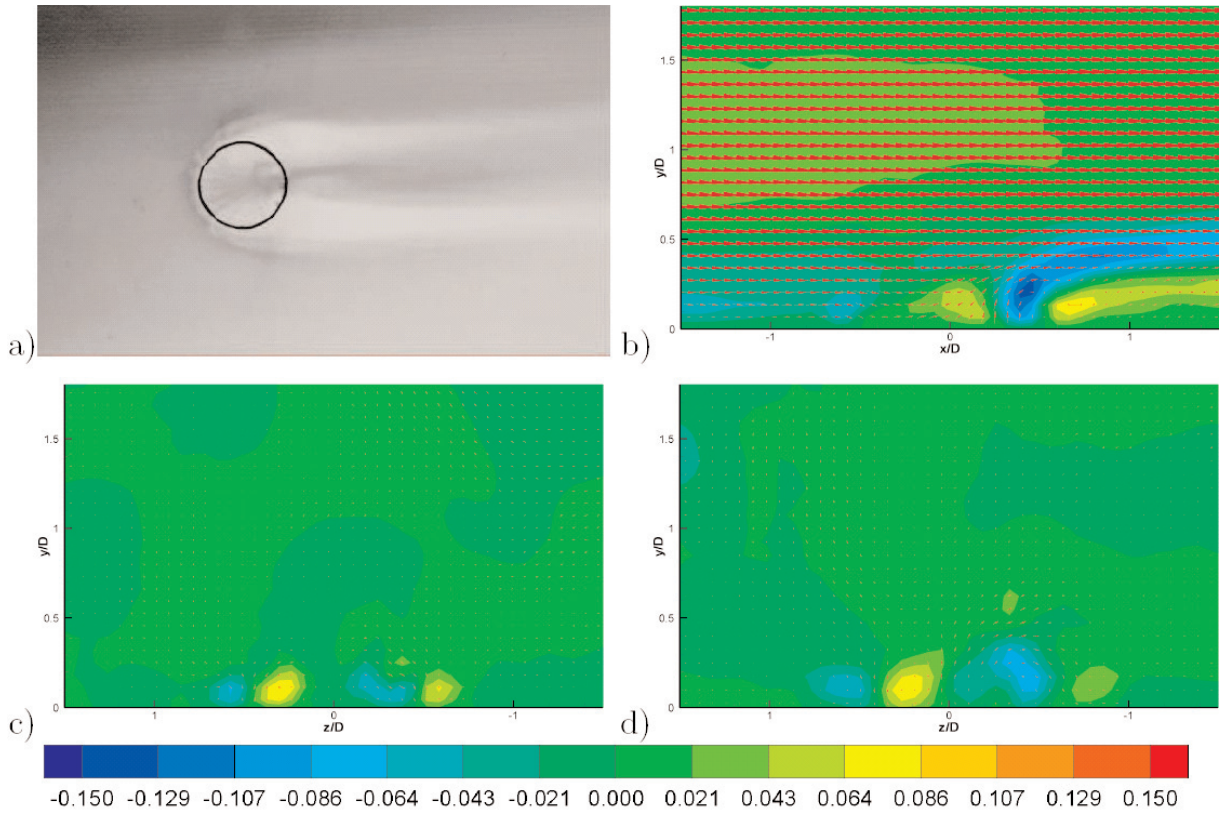


Figure 13. Flow visualisation and time-averaged PIV, St = 46·0.
(a) Flow visualisation; (b) streamwise plane along dimple centre-line; (c) spanwise plane *x/D* = 0; (d) spanwise plane *x/D* = 0·5.

https://doi.org/10.1017/S0001924000004887 Published online by Cambridge University Press

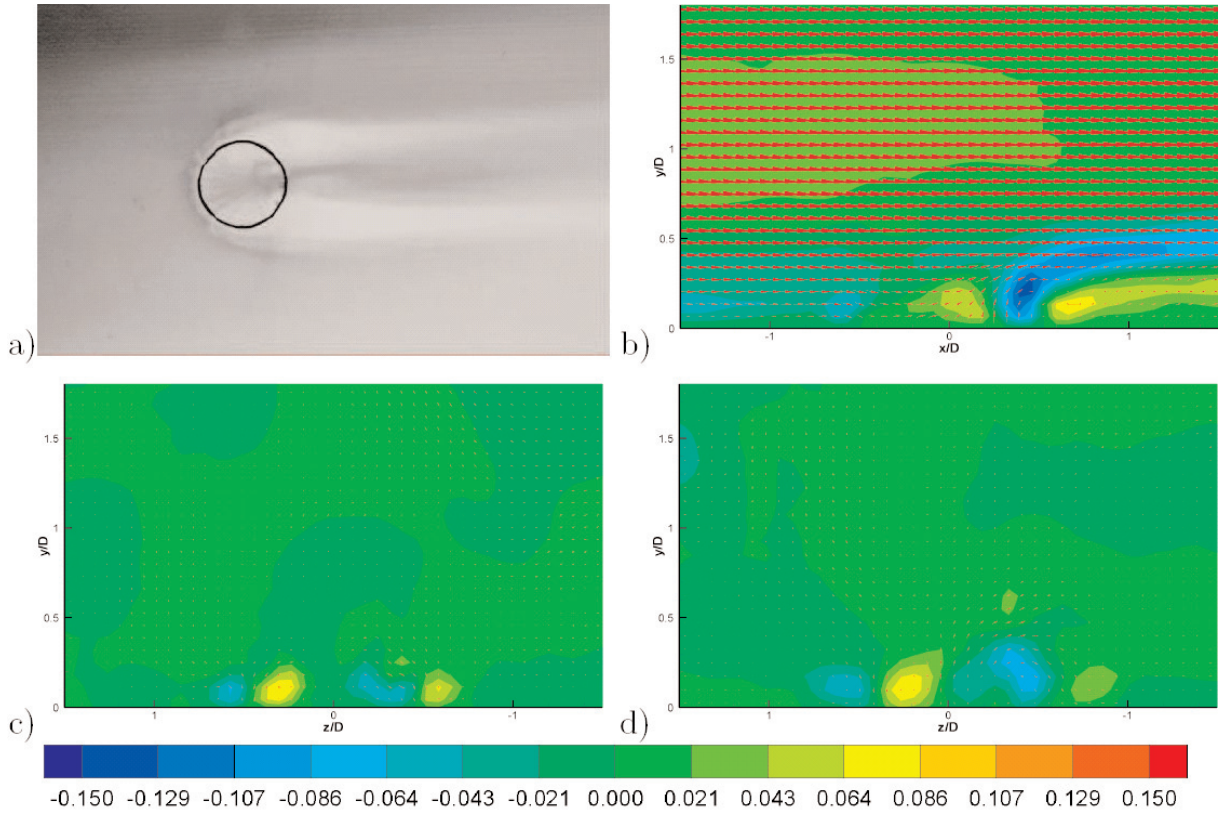


Figure 14. Flow visualisation and time-averaged PIV, St = 112·0.
(a) Flow visualisation; (b) streamwise plane along dimple centre-line; (c) spanwise plane *x/D* = 0; (d) spanwise plane *x/D* = 0·5.

At St = 46·0, another horseshoe-like vortex becomes apparent most clearly seen in the contours of ω_x^* in Figs 14 (c,d). Now, a pair of contra-rotating vortices is apparent on either side of the dimple such that there is common flow towards the surface between the vortices. The origin of the inner horseshoe vortex is shown in the contours of $\omega_z^* - \omega_{z0}^*$ in Fig. 13(b): clearly, the motion of the piston leads to the generation of vorticity on the vertical walls of the vertical-sided dimple. Phase-averaged vorticity contours show that the vorticity is surprisingly persistent throughout the dimple cycle. A further feature at this frequency is that the wrinkling of the outer horseshoe vortex immediately upstream of the dimple. The Reynolds number based on the maximum dimple velocity is approximately 1,500, and is typical of that at which waves first appear on laminar vortex rings. At higher frequencies, the edges of this horseshoe vortex become highly contorted.

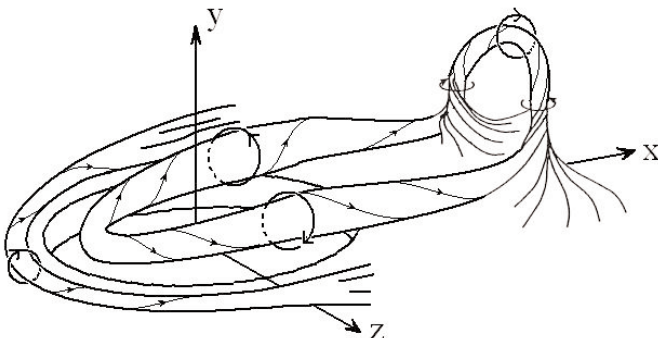


Figure 15. Schematic of modelled flow for the vertical-sided dimple at high frequency[3].

With further increases in frequency (St = 112·0, Fig 14), there appear to be no major structural changes. The horseshoe-like structures become more clearly defined, and in particular, the vorticity generated on the inside faces of the dimple appear to be persistent and highly organised: thus while the velocity vectors change through 180º over a cycle, the vorticity contours show very little variation through the cycle. From Figs 14(b,d), it is clear that the vorticity contours persist out to nearly the edge of the boundary layer, $\delta^* \approx 2$ In Fig. (4), a 'penetration depth' has been defined, based on the conservation of mass flux from the dimple. For this dimple, it is estimated to be $\approx 0{\cdot}2D$ or $\approx 0{\cdot}1\delta$. A model that is consistent with the above is shown in Fig. 15. Further details are given in Refs (3,4).

4.2 Smooth dimple

Practically, EAP-fabricated dimples are more likely to have cross-sectional profiles that have continuous curvature rather than a vertical-sided cross-section. Figure 16 shows the corresponding time-averaged PIV vorticity contours from measurements at corresponding Reynolds numbers (table 2) where the piston is covered in a diaphragm and the amplitude is set to be the same as that for the vertical-sided dimple.

Figure 16 shows time-averaged vorticity contours in the same sequence as that for the vertical-sided dimple. These results are, in fact, typical of any frequency. In this case, any separation would depend on both ε^* and Reynolds number, and on the evidence of Fig. 15, it would appear that, for the conditions investigated here, separation is unlikely. Phase-averaged vorticity contours show that the vorticity generated on the downstroke and upstoke half-cycles is equal and opposite and therefore cancels when averaged over the complete cycle. This also occurs in Stokes' 'second problem', the motion induced in an otherwise quiescent fluid by a flat plate executing simple harmonic motion, the phenomenon occuring because the relevant equation of motion contains

https://doi.org/10.1017/S0001924000004887 Published online by Cambridge University Press

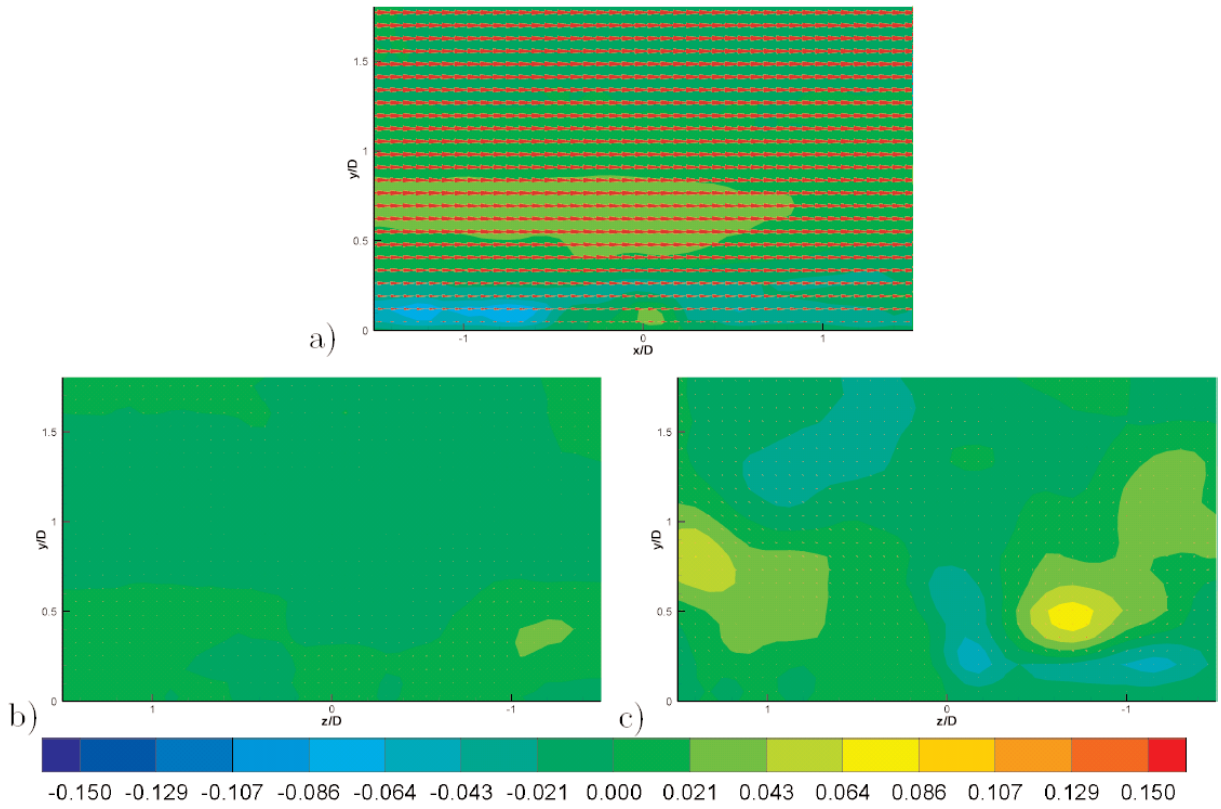


Figure 16. Time-averaged PIV, St = 13·0 – 112·0. (a) streamwise plane along dimple centre-line; (b) spanwise plane *x/D* = 0; (c) spanwise plane *x/D* = 0·5.

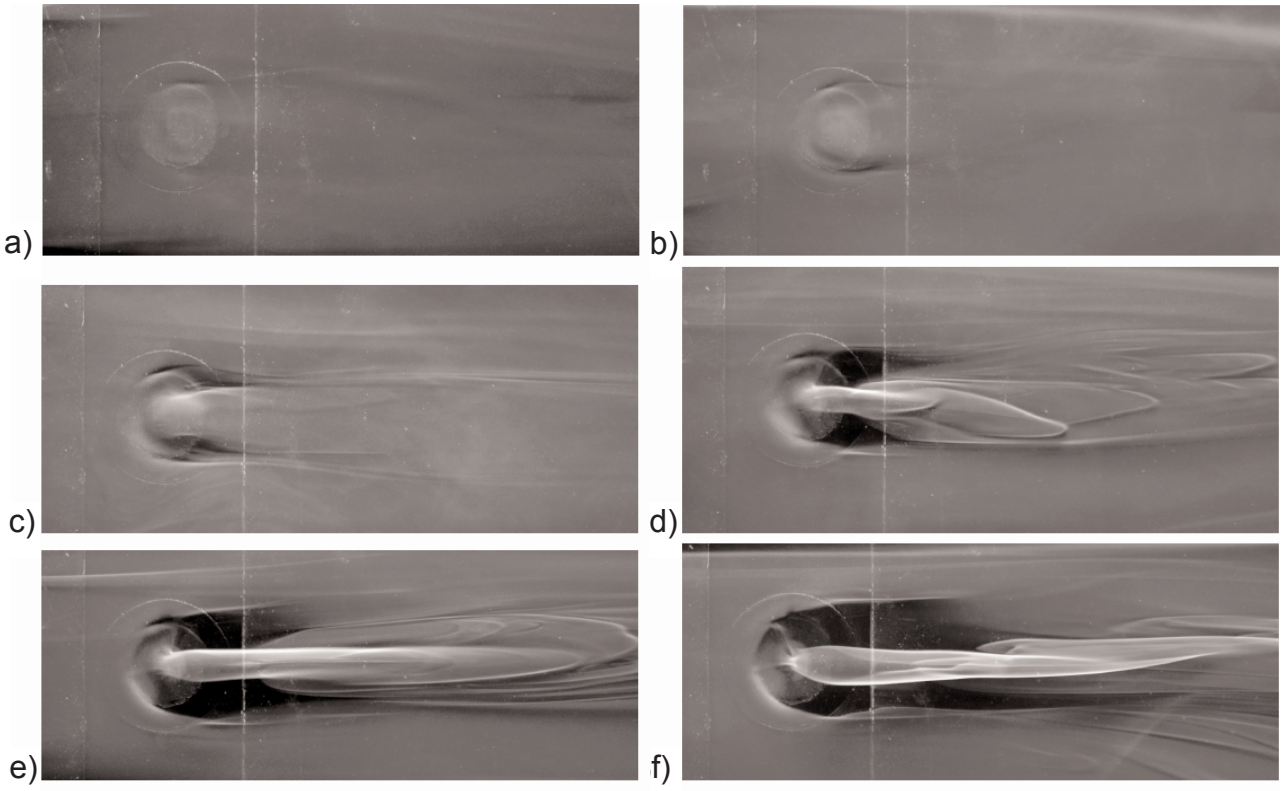


Figure 17. Flow visualisation: (a) St = 13·0; (b) 24·0; (c) 46·0; (d) 68·0; (e) 90·0; (f) 112·0.

https://doi.org/10.1017/S0001924000004887 Published online by Cambridge University Press

no nonlinear convective terms. This would suggest that, in the smooth dimple examples here, no separation occurs either.

Figure 17 shows the corresponding flow visualisation in the (*x,z*)-plane. Here it is clear that the effect of the forcing is primarily to generate streamwise vorticity where, in the dark regions immediately downstream of the dimple, dye is swept towards the centre-line where there is common flow away from the surface. The corresponding phase-averaged contours of the vorticity confirm this. It is likely that there is a spanwise connecting loop at the upstream end, near the leading edge of the dimple. More interestingly, the phase-averaged vorticity contours show that the vorticity moves in phase with the velocity field, with opposite-signed vorticity being generated in each half-cycle. The phase-averaged vorticity magnitudes, which are approximately half those for the vertical-sided dimple indicate that the vorticity is confined to the inner 25% of the boundary layer. It appears then, that, in the case of the smooth dimple, the vorticity, in terms of magnitude and duration, is easier to control than in the case of the vertical-sided dimple: not only can vorticity generation be turned either 'on' or 'off', but also its magnitude may be varied at will by approriate combinations of Stouhal number and Reynolds number.

5.0 CONCLUSIONS

Although the application of EAP to the development of sensors and actuators appropriate for flow control is still in its infancy, it appears suitable for control applications in realistic environments. It has high electro-mechanical efficiency, offers suitably large deflections at high frequencies for it to be considered further. The electro-mechanical validation of EAP membranes for actuation continues in order to understand how these materials behave and to establish a body of working experience. Mechanical tests have shown that spin-coated samples do not necessarily have the same properties as the bulk material. It has also been found that the Shore A number of elastomers affects the electro-mechanical response which can be increased by using modulated dc excitation. More recently, work has begun on the development of EAP for both shear-stress and pressure sensing. Ink-jet printing has been identified as offering a low-cost fabrication technique that offers precision and reliability in manufacture, as well as being extendable to providing distributed organic electronics for control.

A comparison of results investigating the effects of dimple forcing by vertical-sided and smooth dimples suggests that the former generate a pair of persistent horseshoe vortices that have common flow towards the surface. Vertical-sided dimples are therefore likely to be appropriate actuators for open-loop forcing for applications such as separation control. However, owing to the persistence of the vortices, such actuators do not offer the control required for closed-loop control. By contrast, smooth dimples generate vorticity that is in phase with the dimple motion and of magnitude that is controllable by the dimple displacement and acceleration. These actuators therefore require further development, particularly in regard to the fluid response to transient forcing, which is more appropriate to the needs of closed-control schemes.

REFERENCES

1. WADSWORTH, D.C., MUNTZ, E.P., BLACKWELDER, R.F and SHIFLETT, G.R. Transient Energy Release Pressure Driven Microactuators for control of Wall-Bounded Turbulent Flows, AIAA-93-3271, AIAA Shear Flow Conference, 6-9 July, 1993, Orlando, FL, USA.
2. BAR-COHEN, Y. Electroactive Polymer (EAP) *Actuators as Artificial Muscles. Reality, Potential and Challenges*, SPIE Press, 2004, Bellingham, Washington, USA.
3. LAMBERT, S., MCKEON, B.J., KOBERG, W.H. and MORRISON, J.F. Fundamental Studies of Active Dimples, Turbulent Shear Flow Phenomena-4, Williamsburg, 2005, pp 283 – 288.
4. LAMBERT, S. and MORRISON, J.F. Fundamental Studies of Active Dimples, 2006, AIAA-2006-3182.
5. MCKEON, B.J., LAMBERT, S., SHERWIN S.J. and MORRISON, J.F. Active dimples for flow control, Advances in Turbulence X, Proceedings of the 10th European Turbulence Conference, Trondheim. CIMNE, Barcelona, Spain, 2004, ANDERSSON, H. I. and KROGSTAD, P.-Å., (Eds), pp 581 – 584.
6. KOBERG, W.H. Simulation of Flow Control Using Active Dimples, PhD transfer report, 2006, Department of Aeronautics, Imperial College, London, UK.
7. GAD-EL-HAK, M. *Flow Control. Passive Active and Reactive Flow Management*, 2000, Cambridge University Press.
8. MORRISON, J.F., DEARING, S.S., ARTHUR, G.G., CUI, Z. and MCKEON, B.J. Fluid flow control using boundary layer control. International Patent Publication, 2006, WO 2006/040532 A1.
9. ARTHUR, G.G., MCKEON, B.J., DEARING, S.S., MORRISON, J.F. and CUI, Z. Manufacture of micro-sensors and actuators for flow control, *Microelectronic Engng*, 2006, **83**, pp 1205 – 1208.
10. SIRRINGHAUS, H., KAWASE, T., FRIEND, R.H., SHIMODA, T. INBASEKARAN, M. WU, W. and WOO, E.P. High-resolution inkjet printing of all-polymer transistor circuits. *Science,* **290**, 2000, pp 2123-2126.
11. Lighthill, M.J. *Introduction. Boundary Layer Theory. In: Laminar Boundary Layers*, ROSENHEAD, L. (Ed), Clarendon Press, Oxford, UK, 1963.
12. WU, J.Z. and WU, J.M. Vorticity dynamics on boundaries, *Adv. in Appl Mech*, 1996, **32**, pp 119-275.
13. WU, J.Z., WU, X.H. and WU, J.M. Streaming vorticity flux from oscillating walls with finite amplitude, *Phys Fluids*, 1993, **5**, (8), pp 1933-1938.
14. PANTON, R.L. *Incompresssible Flow*, 3rd Ed, 2005, Wiley and Sons, Hoboken, New Jersey, USA.
15. HEDYT, R., KORNBLUH, R., PELRINE, R. and MASON, V. Design and performance of an electrostrictive polymer-film acoustic actuator, *J Sound and Vibration*, 1998, 2152, pp 297-311.
16. PELRINE, R., KORNBLUH, R., JOSEPH, J. HEYDT, R., PEI, Q. and CHIBA, S. 2000 High-field deformation of elastomeric dielectric actuators, Materials Science and Engineering C11 89-100, 2000.
17. LEE, S., JUNG, K., KOO, J., LEE, S., CHOI, H., JEON, J., NAM, J. and CHOI, H. Braille display device using soft actuator. Proc SPIE Int Soc Opt Eng, 2004, 5385, 368.
18. PIMPIN, A., SUZUKI Y. and KASAGI N. Micro electrostrictive actuator with metal compliant electrodes for flow control applications, 17th IEEE Int Confw MEMS, 2004, Maastrict, Netherlands, pp 478-481.
19. WILLIAMS, J.G. *Stress Analysis of Polymers*, Ellis Horwood Series in Engineering Science, 1980, 2nd ed.

https://doi.org/10.1017/S0001924000004887 Published online by Cambridge University Press